WELDING RESEARCH

Microstructure and Impact Toughness of A516 Grade 70 Steel Joints Welded using DF-Modulated P-GTAW Followed by SAW

A fully penetrated 5 mm root pass weld — about 2.5 times deeper than with conventional GTAW — without backing was achieved

BY G. ZHANG, B. ZHANG, N. LV, Y. XU, Y. GU, AND Y. SHI

Abstract

To enhance the quality and production efficiency of welding medium-thick A516 Grade 70 steel, a novel dual-frequency modulated pulsed gas tungsten arc welding technique was proposed to achieve deep penetration on the large root face without backing. Additionally, submerged arc welding was employed for filler and cover welding, further reducing the welding time and optimizing the microstructure of the welded joints. The impact toughness of the welded joints was evaluated and correlated with the microstructural changes. Results indicated that a fully penetrated root pass weld with a depth of 5 mm was successfully achieved. During one-pass filler welding, the weld metal exhibited superior impact toughness compared to the heat-affected zone (HAZ), which was attributed to reduced grain size and an increased proportion of acicular ferrite. Conversely, in two-pass filler welding, the HAZ exhibited higher impact toughness than the weld metal, reaching 107 J, due to the formation of strip-like bainite that impeded crack extension. This study demonstrated the feasibility of the proposed method for achieving high-quality and efficient welding of A516 Grade 70 steel.

Keywords

- Medium-Thick Steel Plates
- GTAW
- Root Pass Welding
- Impact Toughness
- Deep Penetration

Introduction

ASTM A516 Grade 70 steel plates are widely used in fabricating pressure vessels for the nuclear waste, oil, gas, and chemical industries, owing to their excellent mechanical properties, corrosion resistance, and weldability. With the rapid expansion of the nuclear power industry, numerous pressure vessels are being manufactured to store the depleted uranium generated during the nuclear fuel reaction process. Traditionally, medium-thick (thickness 4 mm ~ 25 mm) A516 Grade 70 steel plates are joined using a compound welding procedure that involves manual tungsten inert gas (GTAW) root pass welding, followed by filler and cover welding. However, this compound process has inherent drawbacks, including a long production cycle, shallow weld penetration, and unstable weld quality in the root pass, which result in inferior joint properties and substantially higher welding costs (Refs. 1–3). To address these issues, many studies have focused on reducing the welding production time of medium-thick steel plates by employing new techniques that increase weld joint penetration. These techniques primarily include plasma arc welding (PAW), keyhole GTAW (K-GTAW), activated GTAW (A-GTAW), high-energy beam welding, and laser hybrid arc welding (Refs. 4–8). The depth-increasing mechanism of these techniques involves significantly enhancing the arc energy density and arc plasma flow force using external devices or a high welding current, thereby effectively pushing aside the liquid fluid metal and leading to keyhole

https://doi.org/10.29391/2025.104.032

formation and full penetration of the substrate (Refs. 9, 10). In high-energy beam welding and laser hybrid arc welding processes, the beam vaporizes the liquid metal of the weld pool, creating a keyhole that transmits more energy into the weld pool bottom to achieve deep penetration, as detailed by Yang et al. (Ref. 11).

The aforementioned techniques possess inherent disadvantages regarding the application of the deep penetration welding process in the fabrication of nuclear pressure vessels. These include complex torch structures of large dimensions that are unsuitable for narrow grooves or conditions requiring large root face passes. Recently, the high-frequency pulsed gas tungsten arc welding (HF-GTAW) technique was considered as a method to weld medium-thick plates due to its larger penetration depth and easier automatic welding process, which has been applied in the root pass welding of thickness plates, for increment of the productivity reported by Kanchan et al. and Dong et al. (Refs. 12, 13). The increased weld penetration was related to energy density enhancement and stronger weld metal fluid flow, which are caused by strong pinch action, higher stiffness, and the force of the electric arc (Refs. 14–16). Success in the performance of multi-layer, multi-pass welded joints primarily depends on factors such as heat input, interlayer temperature, and choice of filler materials (Refs. 17–19). Therefore, maintaining a minimum necessary heat input and optimal cooling rate of the weld pool is crucial for achieving high performance and shortening the welding production cycle.

Investigations have reported that the impact toughness of A516 Grade 70 steel welds is highly sensitive to the welding thermal cycles, which may include large heat input with rapid cooling rates, multi-layer and multi-pass welding processes using identical welding parameters, and high-preheat treatments (Refs. 20–22). Moreover, literature published by Chen et al. (Ref. 23) reported that the average Charpy impact energy of weld joints used in nuclear pressure vessels should exceed 31 J at –46°C, with each specimen not measuring lower than 25 J. During the multi-layer multi-pass welding process, the heat-affected zone (HAZ) of the weld joint experiences multiple thermal cycles, resulting in a distinction of the microstructure and impact toughness. Studies reported that acicular ferrite (AF) tends to nucleate preferentially at non-metallic inclusions such as Ti_2O_3, TiO_2, MnO, and SiO_2 particles, effectively enhancing the impact toughness of the weld metal (Refs. 24–26). Luo et al. (Ref. 27), Huda et al. (Ref. 28), Li et al. (Ref. 29), and He et al. (Ref. 30) have reported that the martensite-austenite (M-A) constituent closely correlates with the impact toughness of welded joints. Although the blocky M-A constituents occupy a small volume fraction and are dispersed, they do not significantly affect the impact toughness of the welded joints. Lath-shaped M-A constituents are prone to solidification cracking because of the volume expansion of martensite and the difference in thermal expansion coefficients between martensite and austenite, resulting in local stress concentration, which reduces the impact toughness of welds. Therefore, the morphology and amounts of M-A constituents should be strictly controlled by adjusting the welding procedure or welding parameters.

To achieve this purpose, a typical Y-groove butt joint with a large root face and a small groove angle was employed in this study to minimize the use of filler materials and increase weld productivity. An enhanced dual-frequency modulated pulsed GTAW (DF-modulated P-GTAW) process was developed to achieve deep penetration on the large root face without backing. Subsequently, submerged arc welding (SAW) was utilized for both filler and cover welding, further reducing welding time and optimizing the microstructure of the welded joints. Three distinct experiments were conducted using different filling and covering procedures, and impact toughness was correlated with microstructural changes.

Materials and Methods

The DF-modulated P-GTAW system, as illustrated in Fig. 1A, consisted of two welding power sources: a low-frequency pulsed supply (Huayuan WSE-315IGB) and a high-frequency pulsed supply (Miller Dynasty® TIG350). The dual-frequency modulation of the current waveform was achieved by fine-tuning the high- and low-frequency pulse parameters of the welding power supplies.

This experiment utilized a workpiece made of A516 Grade 70 steel with dimensions of 500 mm × 100 mm × 16 mm. The angle, root face, and root gap of the Y-groove butt joint are illustrated in Fig. 1B. The compositions of the materials employed in this study are presented in Tables 1 to 3. In the welding procedure, the Huayuan ZD5-1000 multi-feature submerged arc welding power source was used to perform the filler and cover welding. The welding parameters are listed in Tables 4 and 5, and the root pass welding process used the DF-modulated P-GTAW without a filler wire for autogenous welding, achieving a fully penetrated weld bead with one-sided welding and back-formation under a constant welding speed of 2 mm/s. Realizing the deep penetration enabled by the dual-frequency modulated pulse arc primarily stemmed from the high-frequency pulsed electromagnetic compression effect. This phenomenon significantly enhances both energy density and arc penetration capability, thereby promoting the formation of a liquid metal film at the bottom of the weld pool and subsequent keyhole development. Moreover, the dual-frequency modulation current waveform concurrently stabilizes energy distribution across the upper and lower regions of the weld pool, effectively reducing the thermal fluctuations, and it establishes optimal thermodynamic equilibrium conditions essential for achieving high-quality one-sided welding with back formation. These combined effects ensure improved process stability and enhanced metallurgical characteristics throughout welding. A series of experiments was conducted on the substrates. Standard V-notch Charpy specimens were machined in accordance with ASTM E23-96, *Standard Test Method for Notched Bar Impact Testing of Metallic Materials*, from the butt-welded joints with their notched roots located in the HAZ and weld metal (WM), as shown in Fig. 2, in which the V-notch root was in the cross-section of the weld bead. Its central line vertically traversed the covering layer, filling layer, and root pass layer in the weld metal specimen, which can be seen in Fig. 2B. The notch central line in the HAZ is illustrated in Fig. 2C; it included the largest area of the HAZ, especially the coarse-grained region. All the specimens were obtained in the same orientation from the

welded joint. These Charpy specimens were tested at –46°C using a drop weight impact tester. To reduce data errors, the average value of the three specimens' measurements was taken as the result.

In accordance with the CN-GB/T 2650-2008 standard, *Impact test methods on welded joints*, Charpy impact tests were performed on standard Charpy V-notch specimens (size: 10 mm × 10 mm × 55 mm) by an NCS NI 300 impact tester of 150 J capacity with an impact velocity of 5.25 m/s in an ambient environment. In accordance with the CN-GB/T2654-2008 standard, hardness tests were conducted on the weld metal and HAZ using a durometer (HAT-1000A). The metallographic sample was roughened and finely ground with SiC paper, followed by polishing and etching.

Table 1 — Chemical Compositions of A516 Grade 70 Steel (wt-%)

Element	C	Si	Mn	Al	S	P	Fe
Content	≤ 0.2	0.15–0.5	1.2–1.6	≥ 0.02	≤ 0.025	≤ 0.012	Ba.

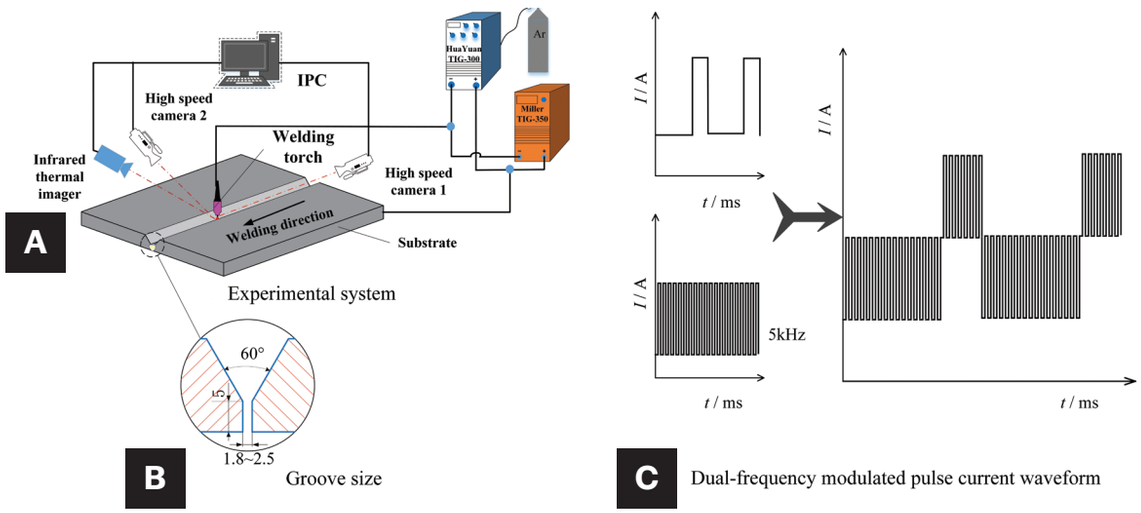

Fig. 1 — Schematic diagram of welding system: A — Experimental system; B — groove size; C — current waveform.

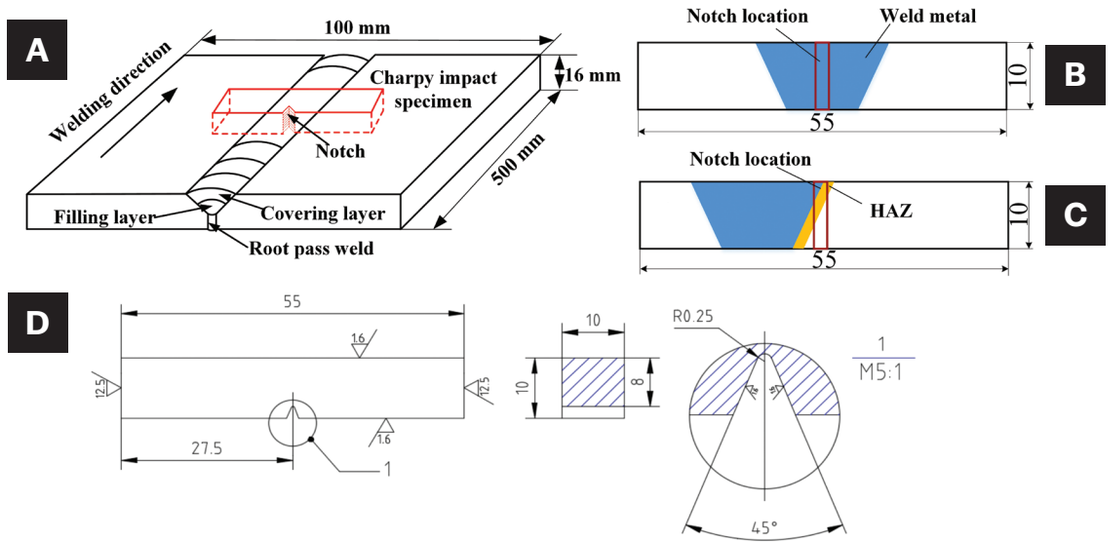

Fig. 2 — Charpy V-notch impact specimen prepared diagram: A — Specimens machined in the weld bead; B — notch location in weld metal; C — notch location in HAZ; D — standard dimension of V-Charpy impact specimen.

The reagent used was a 4% nitric acid alcohol solution. After preparing the metallographic sample, a laser confocal microscope (LSM800) was employed to observe the microstructure of the root pass welds. Additionally, a scanning electron microscope (SEM, FEI Nova nano SEM) was used to observe and analyze the joint microstructure, the HAZ and the distribution of second phases and inclusions. Furthermore, an energy dispersive spectrometer (EDS, X-Max 150; Oxford Instruments, UK) was utilized to quantitatively characterize the distribution of relevant elements under an accelerating voltage of 20 kV, a working distance of 10 mm, a beam current 0.5–10 nA and live time of 30 ~ 60 s for the main element and 100-300 s for the microelement. The expected error in the measurements was set as followings: total error (sum of the contents of all elements) ≤ ±3%, main element (> 20 wt-%) ≤ ±5%, medium content

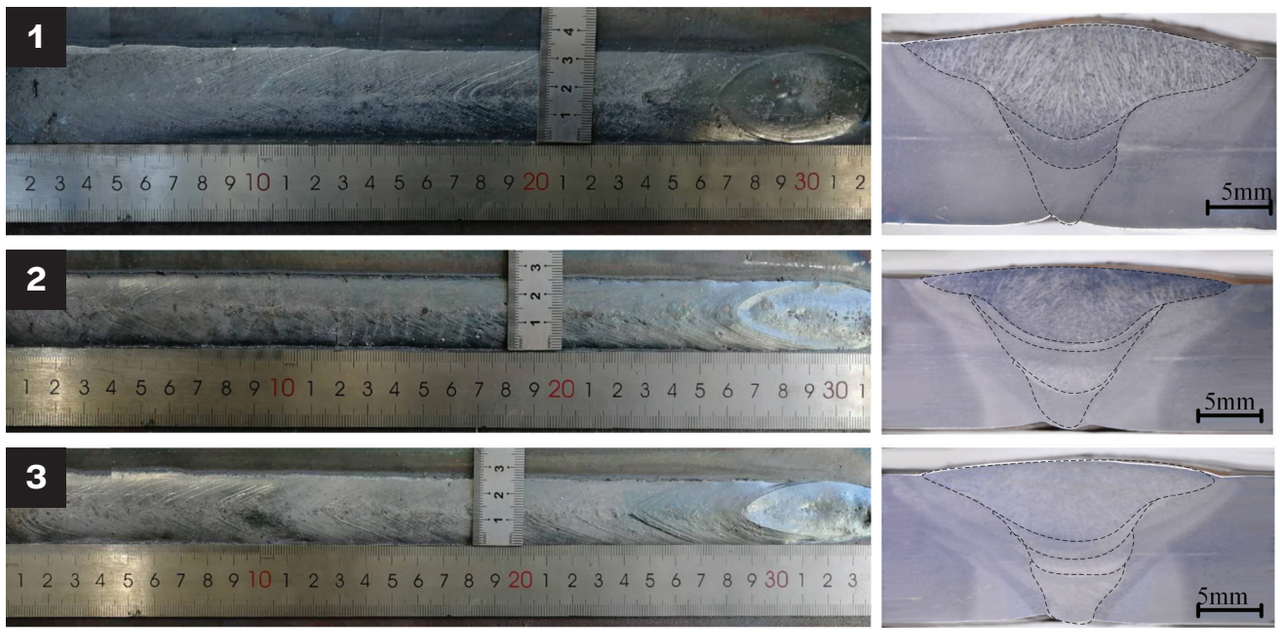

Fig. 3 — Weld bead formation and cross sections.

Table 2 — Chemical Composition of H10Mn2 Filler Wire (wt-%)

C	Si	Mn	Ni	V	Cr	Mo	S	P	Fe
0.12	0.07	1.5	0.3	—	0.2	—	0.035	0.035	Ba.

Table 3 — Chemical Composition of SJ101 Flux (wt-%)

Alkalinity	$SiO_2 + TiO_2$	$CaO + MgO$	$Al_2O_3 + MnO$	CaF_2
1.8	25	30	25	20

Table 4 — Root Pass Welding Parameters

Low Frequency Current				High Frequency Current			
Peak current/A	Base current/A	Frequency /Hz	Duty-cycle /%	Peak current /A	Base current /A	Frequency /Hz	Duty-cycle /%
310	180	1.5	20	190	95	5000	50

Table 5 — Filler and Cover Welding Parameters

No.	Procedure	Current/A	Voltage/V	Welding Speed mm/s	Interlayer Temperature/°C	Heat Input / kJ/cm	Average Heat Input/ kJ/cm	Filler Wire
1	Filling	560	30	4.3	—	33.24	42.56	H10Mn2
	Covering	630	31	3.2	170	51.88		
2	First filling	520	28.1	5	—	24.84	22.40	H10Mn2
	Second filling	412	24	5.7	100	14.75		
	Covering	580	28	5	200	27.61		
3	First filling	410	23.8	5.7	—	14.55	21.91	H10Mn2
	Second filling	515	27.2	5	100	23.81		
	Covering	577	27.9	5	200	27.37		

element (3–20 wt-%) ≤ ±10%, low content (1–3 wt-%) ≤ ±30%, microelement (0.5–1 wt-%) ≤ ±50%.

The temperature cycles occurring during welding (temperature-time curve) influence the mechanical properties in the WM and HAZ. The cooling time $t_{8/5}$ is the time required during the cooling of a weld bead and its HAZ to pass through the temperature range from 800°C to 500°C, which can be calculated using the following equation (Ref. 31) due to the application of medium-thick plates in this study.

$$t_{8/5} = \left(0.67\text{-}5\times10^{-4}T_0\right)\eta \times E\left(\frac{1}{500\text{-}T_0}\text{-}\frac{1}{800\text{-}T_0}\right) \times F_3$$

where T_0 is preheat temperature, F_3 is the seam factor for three-dimensional heat dissipation, η is thermal efficiency, and E is energy input. In this study, $\eta = 0.9$, $F_3 = 0.9$, and $T_0 = 58.6$°C.

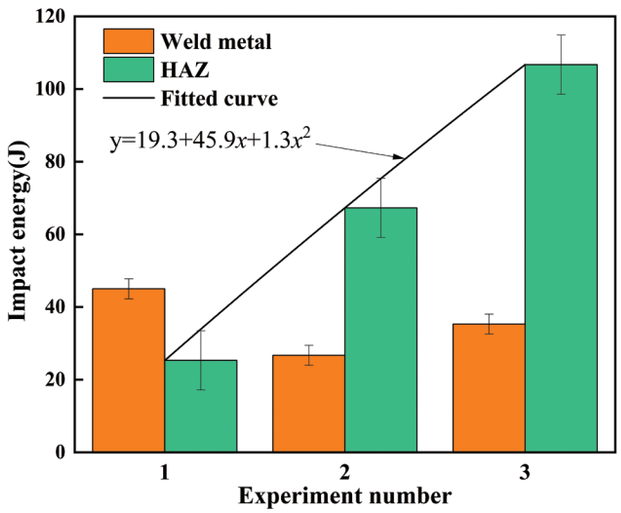

Fig. 4 — Impact energy of weld joints.

Results

Macroscopic of Weld Beads with Different Welding Procedures

Figure 3 illustrates the morphologies and cross-sections of the welded joints. A single-pass filler welding procedure was employed in Experiment 1. The thickness of the filler pass layer was relatively small (~ 2 mm), necessitating a higher welding current (630 A) for the covering pass. As a result, the top width of the weld bead reached approximately 33 mm, with a bead height ranging from 2.5 to 3 mm. Furthermore, the large heat input contributed to a wider HAZ. The morphologies of welds two and three demonstrated a significant increase in the thickness of the filled weld. This was attributed to the relatively smaller welding current (577 A) used in the cover welding process, which reduced the weld width. The top width and height of the weld bead were approximately 25 mm and 2.5 mm, respectively. Additional comparisons revealed that when a smaller welding current was used in the initial filling process, the overall width of the filling weld bead was reduced and the HAZ was also relatively narrower. These observations suggest potential benefits for enhancing the joint properties.

Impact Toughness of Welded Joints

The impact toughness of the weld metal and the HAZ were tested, and the results are listed in Table 6. The average impact toughness of the weld metal and the HAZ in three

samples, obtained from the same weld bead at different locations, was calculated and plotted.

As can be seen from Fig. 4, in the first experiment, a large average heat input (42.56 kJ/cm) was applied, and the impact toughness of the weld metal was higher than that of the HAZ. In the second and third experiments, a small average heat input (~ 22 kJ/cm) was applied, and the impact toughness of the HAZ was higher than that of the weld metal. Furthermore, when a smaller heat input (14.55 kJ/cm) was applied in the first filling pass, the impact toughness of the HAZ was enhanced to 107 J, and the impact toughness of the weld metal had a slight increase to 35 J. The comparison between the second and third experiments indicate that a good weld joint with higher impact toughness can be obtained when a smaller heat input (14.55 kJ/cm) is applied in the first filler welding procedure (Experiment 3), which well meets the requirement of 31 J at –46°C of the nuclear pressure vessels.

Microstructure Characterization

Microstructure of Root Pass Weld Bead Without Heat Action of Filler Welding Process

Figure 5A illustrates the macroscopic structure of the root pass weld bead obtained by only the DF-modulated P-GTAW process. The weld metal (WM) shown in Figs. 5B and C comprised a small amount of mixed structure of acicular ferrite (AF) and pearlite, which is known as the Widmanstatten structure (W). The pearlite was distributed in the AF lath layer, and its proportions were nearly identical. Figure 5D shows the coarse-grained HAZ (CGHAZ) in which martensite (M), W, and some coarse dendrites were formed. Figure 5E presents the fine-grained HAZ (FGHAZ); however, the grain size slightly increased due to the excessive heat input, and

Table 6 — Impact Toughness Value of Weld Joints (at –46°C)

No.	Weld Metal			HAZ		
	Sample 1	Sample 2	Sample 3	Sample 1	Sample 2	Sample 3
1	43	48	47	22	25.8	28.1
2	29	28	23	59	66.7	75.9
3	34	37	35	111	103	106

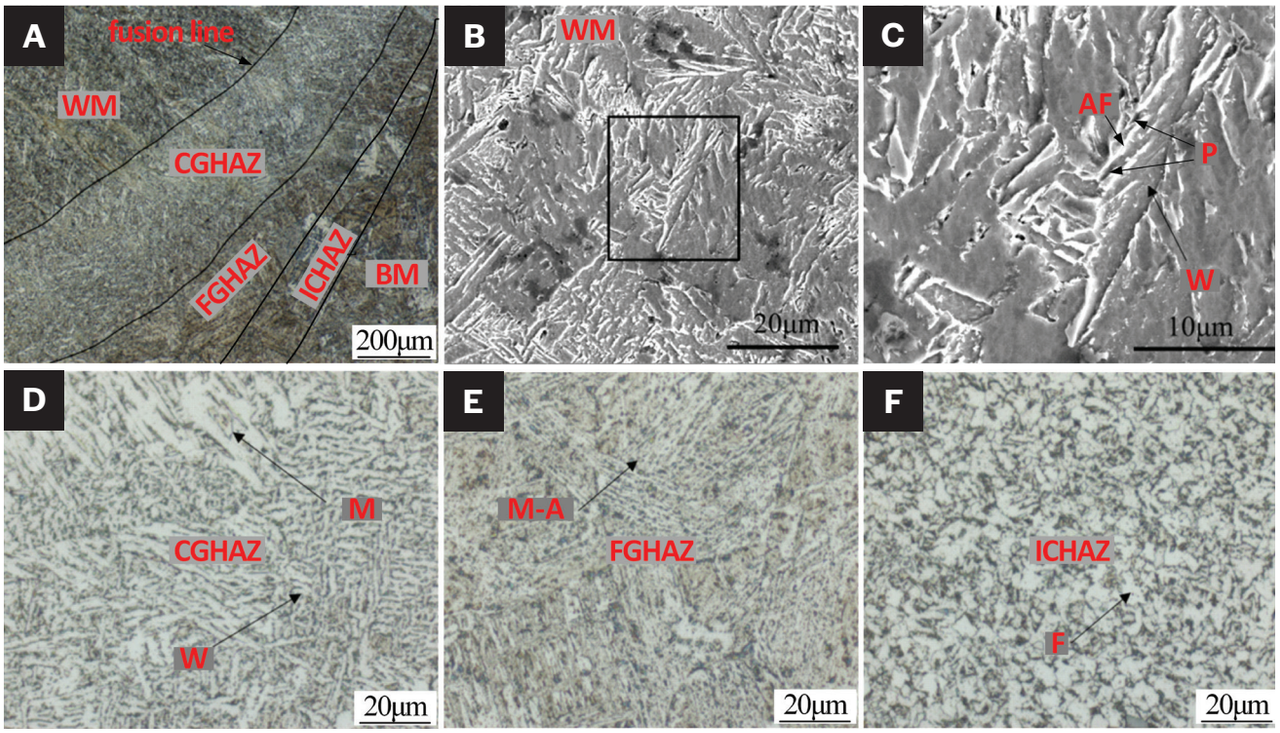

Fig. 5 — Microstructure of root pass weld bead: A — Macroscopic feature; B — weld metal center; C — enlarged area; D — CGHAZ; E — FGHAZ; F — ICHAZ.

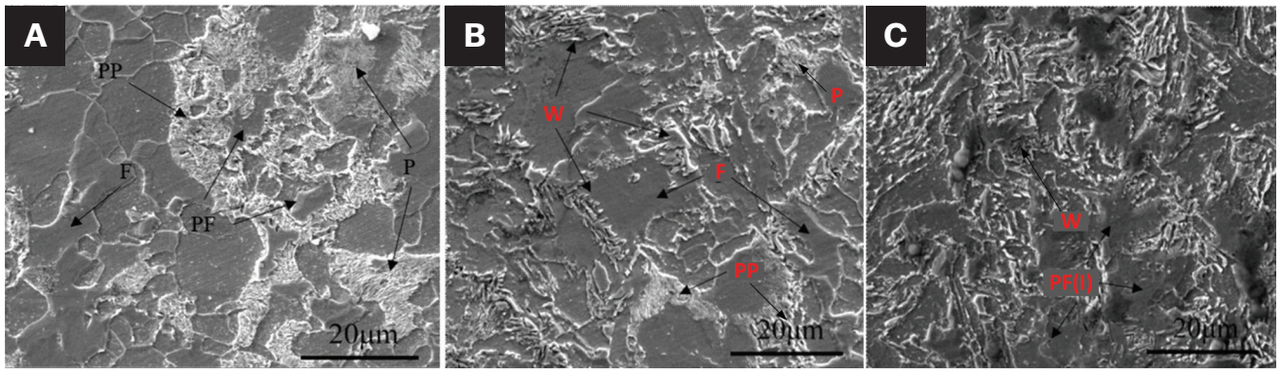

Fig. 6 — Microstructure of the root pass weld bead under different heat inputs: A — ~ 33 kJ/cm; B — ~ 25 kJ/cm; C — ~ 14 kJ/cm.

a small amount of martensite-austenite (M-A) constituent was generated in the austenite grain. Moreover, the blocky M-A was distributed between the bainite and ferrite slats, which might have deteriorated the impact toughness. Figure 5F shows the intercritically reheated HAZ (ICHAZ), in which the ferrite grain size increased and the distribution of pearlite and ferrite occurred.

Microstructure of Welded Joints

Filler and cover welding were conducted on the root pass weld bead using the parameters in Table 5. Two kinds of experiments were performed to optimize the microstructure of the root pass layer: two-pass filler welding followed by one cover welding and one-pass filler welding followed by one cover welding. Because of the thermal cycle action of filler welding on the root pass weld bead, the bottom microstructure of the weld joints could be changed; hence, the microstructural evolution of the root pass weld bead under different heat inputs of the filler welding process was first analyzed, as shown in Fig. 6.

Figure 6A reveals distinct microstructural characteristics in the weld metal under a high heat input condition (~ 33 kJ/cm) during the filler welding process (Experiment 1). The microstructure predominantly consisted of pseudo-pearlite (PP) with minor pearlite and ferrite phases, accompanied by sporadic primary ferrite (PF) precipitates embedded within the pearlite matrix. PP originates from undercooled austenite deviating from the eutectoid composition during cooling, manifesting as irregular granular structures randomly dispersed in the ferrite matrix. This phenomenon can be attributed to three interrelated factors: 1) the heterogeneous cooling rates between the weld pool center and edge under varying heat inputs create significant thermal gradients; 2) these thermal gradients enhance the degree of undercooling while simultaneously reducing carbon diffusivity in austenite; 3) the combination of reduced diffusion mobility and carbon redistribution limitations leads to non-uniform carbon partitioning. Moreover, the suppressed long-range carbon diffusion has two critical consequences: progressive depletion of pearlitic lamellae formation, driving the system further from equilibrium eutectoid composition, and delayed pearlite transformation kinetics that increasingly deviate from the equilibrium eutectoid temperature. When the transformation temperature falls below the metastable eutectoid threshold, cementite precipitation occurs through a discontinuous mechanism. Rather than forming characteristic continuous lamellae, cementite particles adopt discrete granular morphologies distributed across the ferrite matrix. This non-lamellar aggregation of cementite and ferrite constitutes the fundamental microstructural signature of pseudo-pearlite.

When a moderate heat input (~ 25kJ/cm, Experiment 2) was applied, the microstructure shown in Fig. 6B changed, generating a substantial amount of W structure and a smaller quantity of PP. Notably, the PP structure was formed in moderate and large heat input conditions. With an increase in heat input, the proportion of W structure decreased while the proportion of PP increased. In the case of small heat input (~ 14 kJ/cm, Experiment 3), the microstructure of the root pass layer underwent minimal transformation and retained a portion of W structure. Some W transformed into intragranular polygonal ferrite (PF(I)), as shown in Fig. 6C, in which the W was distributed in a ring around the ferrite grains. Consequently, the microstructure of the root pass layer could be optimized by controlling the heat input used in the filler welding process, where the numerous W structures could be eliminated, and more AF and pearlite were generated, which may improve the impact toughness of the weld metal.

The microstructures of weld joints with different filler welding procedures were also observed and are shown in Fig. 7. Under the two-pass filler welding condition, the weld metal microstructure consisted of grain boundary ferrite (PF(G)), AF, and a small amount of W structure dissolved from the grain boundary, and the prior austenite grains grew, as shown in Fig. 7A. Under the one-pass filler welding condition, the microstructure of the weld metal was almost the same as the two-pass filler welding case, but there were some minor changes, such as fine PF(G), no W, and a higher proportion of AF (qualitative estimation in the field range of the SEM), as shown in Fig. 7B. However, the HAZ microstructure of the two-pass filler welding applied joint shown in Fig. 7C included upper bainite, granular bainite and a small amount of pearlite when the cooling time $t_{8/5}$ was 10 s. In the one-pass filler welding condition with a lower cooling rate ($t_{8/5}$ = 14 s), the HAZ microstructure consisted of lower bainite and a small amount of pearlite, as shown in Fig. 7D.

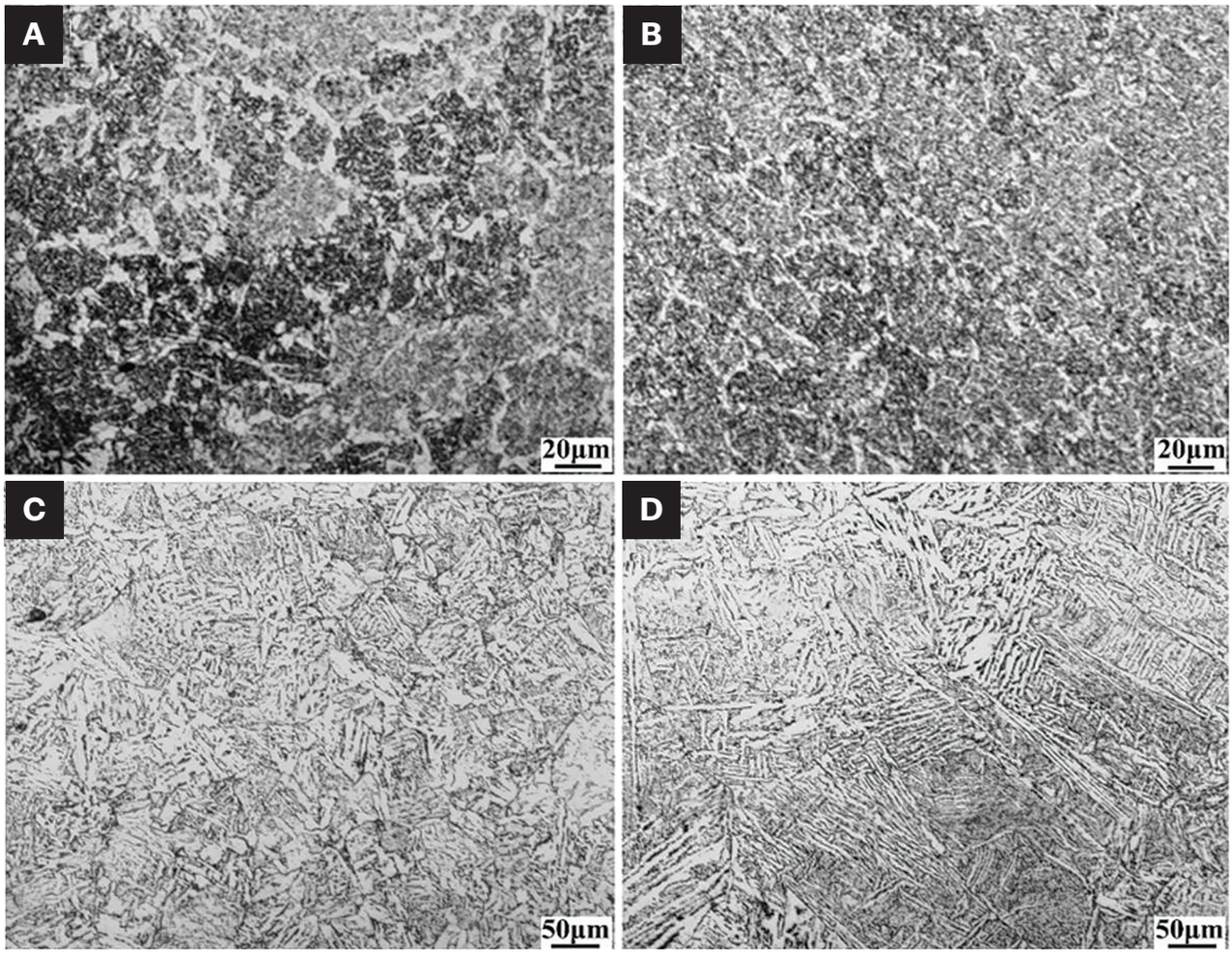

Fig. 7 — Microstructure of the welded joints under different filler welding procedures: A — Central microstructure of weld metal in two-pass filler welding condition; B — central microstructure of weld metal in one-pass filler welding condition; C — HAZ microstructure in two-pass filler welding condition ($t_{8/5}$ = 10 s); D — HAZ microstructure in one-pass filler welding condition ($t_{8/5}$ = 14 s).

To elucidate the formation mechanism of AF, the morphology and chemical composition of AF were characterized using electron probe microanalysis (EPMA) combined with EDS. The nucleation and growth processes were analyzed in detail, as shown in Fig. 8.

As illustrated in Fig. 8A, non-metallic inclusions were observed on the ferrite grain boundaries. It was stated that the average diameter of non-metallic inclusion was 1.38 μm, which satisfies the size criterion for the nucleation of acicular ferrite (≥ 0.2 μm) (Ref. 32). The element mapping and atomic percentages are presented in Figs. 8B–G. Oxygen (O), titanium (Ti), manganese (Mn), and silicon (Si) elements were segregated and enriched within the inclusions. Combined EDS and EPMA analyses revealed that the inclusions exhibited an internal structure comprising complex oxide phases, with Ti and Mn identified as primary constituents forming core regions. These metallic cores were enveloped in oxide matrices similar to TiO and $(Ti, Mn)_2O_3$ compositions. The EDS result further confirmed the presence of sulfur (S) within the interior of the inclusions.

Publications (Refs. 33, 34) have reported that the nucleation of acicular ferrite (AF) in Mn-included steel is closely associated with the elements present in the inclusions. Inclusions with $(Ti, Mn)_2O_3$ cores readily absorb the surrounding Mn and S elements, leading to the formation of MnS on the surface of the oxides. Thus, the presence of S elements in the inclusions was evident from the EDS result. Mn, as a stabilizing element for austenite, is readily absorbed by the inclusions, resulting in a depletion of Mn elements around the inclusions and the subsequent formation of Mn-depleted zones. The formation of these Mn-depleted zones increases the temperature required for the transformation of austenite to ferrite and reduces the nucleation resistance of ferrite

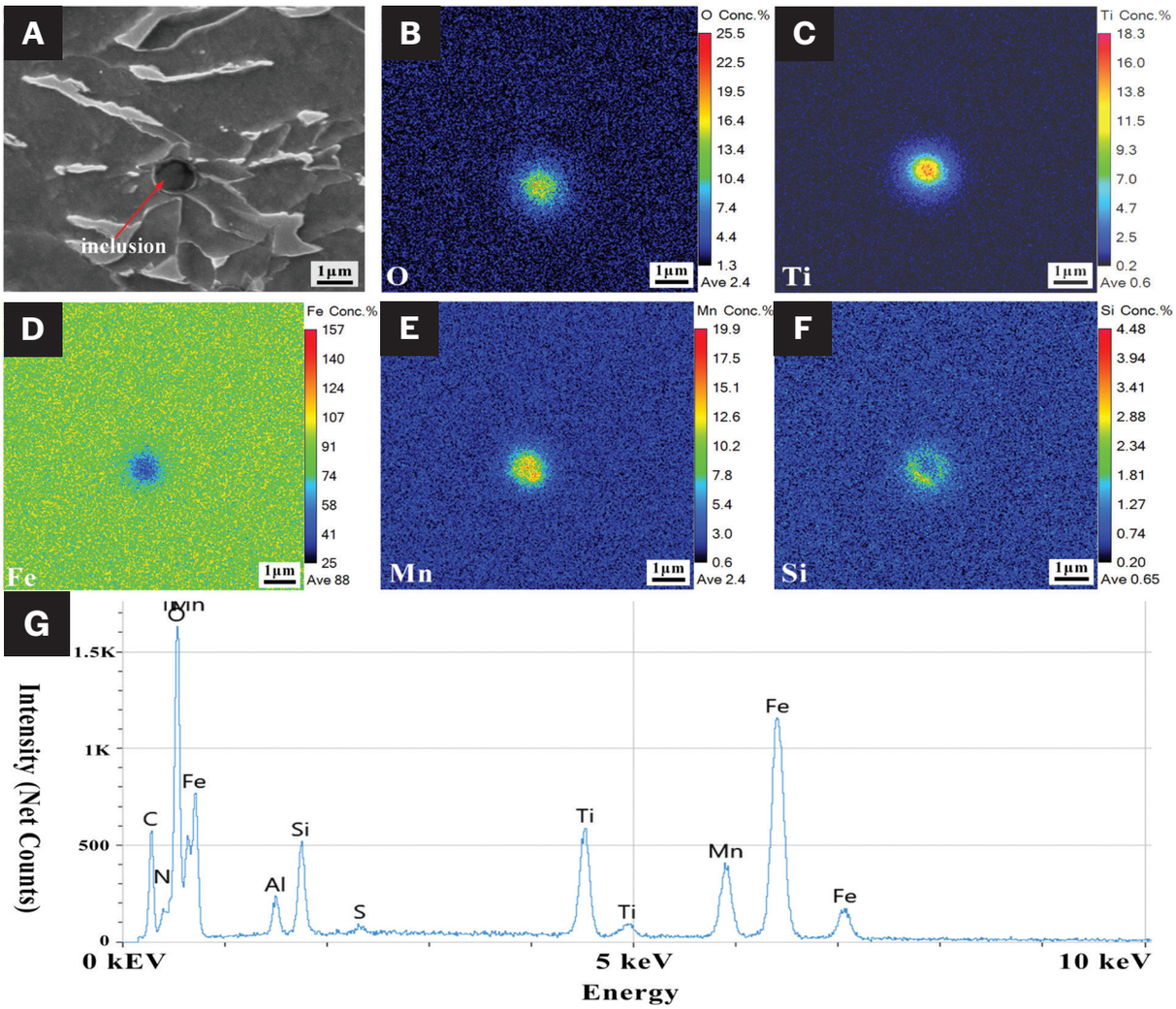

Fig. 8 — Intracrystalline inclusions and element mapping: A — Microstructure of inclusions; B–G — EDS and EPMA result.

(Ref. 35). Consequently, AF is more likely to nucleate at and around non-metallic inclusions.

Fracture Morphologies of Impact Test Specimens

Figures 9A(A–D) present the macroscopic and microscopic morphologies of the central fracture section of the weld metal along with an enlarged view of the microscopic morphology. The fracture exhibited a significant proportion of fibrous region and shear lips, indicating the occurrence of lamellar tearing during impact fracture. The relationship between them has been reported in the literature (Refs. 36, 37). Numerous small dimples containing inclusion particles were observed on the fracture surface, indicative of void coalescence ductile fracture. Figures 9A(E–H) show the macroscopic and microscopic morphologies of the central fracture section in the HAZ. The fracture surface of the impact specimen displayed an inverted cone-shaped morphology. The cross-section of the fracture varied considerably, featuring an uneven and rugged surface. The fibrous region occupied a relatively large proportion, and a prominent shear lip formed an approximate 45 deg angle with the component surface. Most of the fracture surface appeared dull and grey, exhibiting evident ductile fracture characteristics. Microscopic examination revealed numerous dimples on the impact fracture surface, which is typical of a ductile fracture and aligns with the measurements listed in Table 6.

Figure 9B (A–D) illustrates the morphologies of the fracture surfaces in the central weld metal, while Fig. 9B (E–H) depicts those of the HAZ. The fracture surface exhibited an inverted cone-shaped morphology, with a high proportion of the fibrous region and shear lip. The microscopic morphology revealed stepped secondary cracks, suggesting layered tearing during the fracture of the impact specimen. The fracture surface was covered with numerous small dimples containing many fine inclusion particles, characteristic of a microporous aggregation-type ductile fracture. However, Fig. 9B (F–H) shows that the fracture section was straight

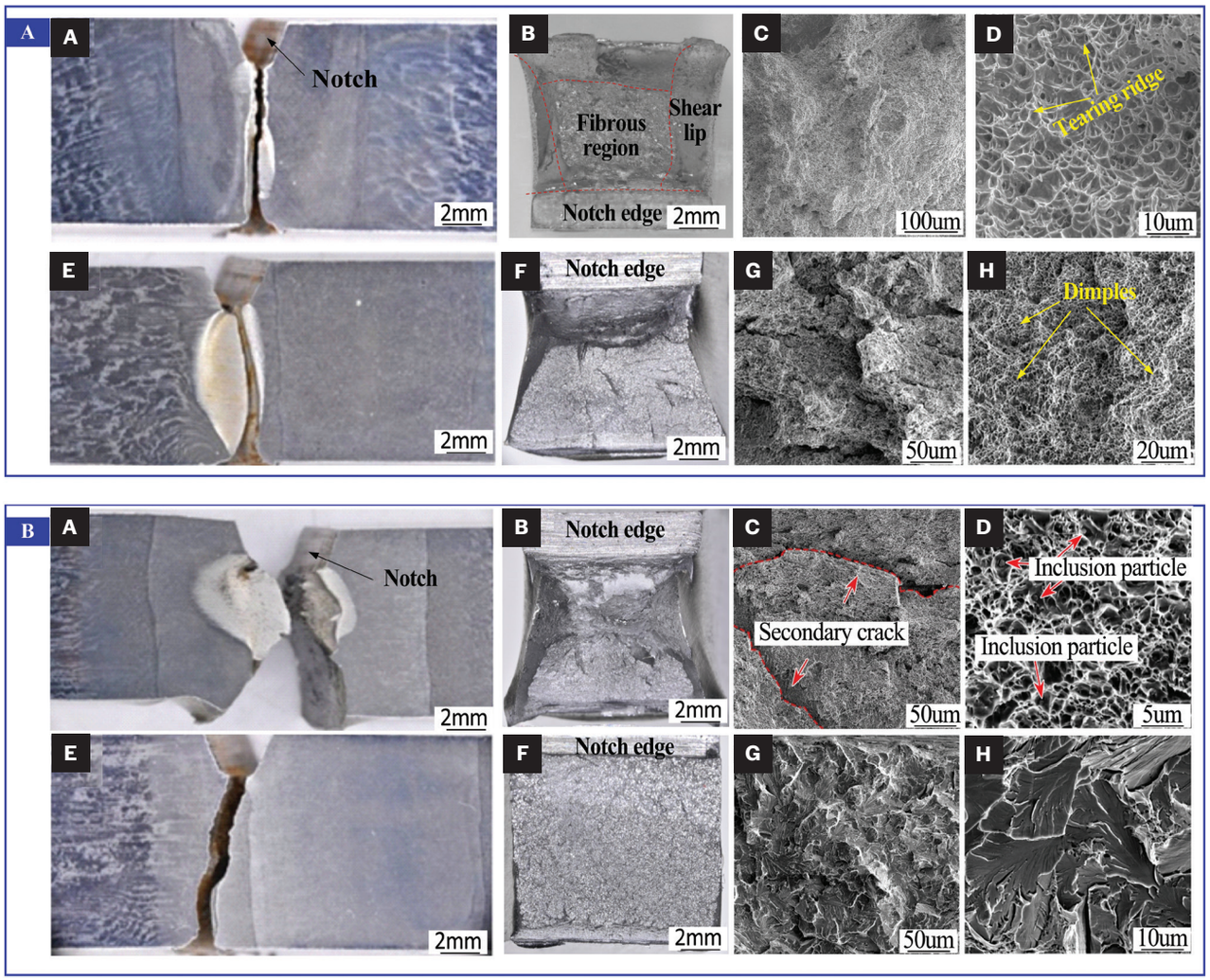

Fig. 9 — Impact fracture morphology: A — With two filler passes welding (Experiment 3); B — with one filler pass welding (Experiment 1).

and almost devoid of any signs of plastic deformation. The fibrous region and shear lip were virtually absent, with the entire area predominantly composed of the radial region. It exhibited a crystalline fracture morphology consisting of sparkling facets. Microscopic examination revealed a river-like pattern, a primary characteristic of cleavage fracture. The cleavage planes were relatively large, indicating a typical brittle fracture.

The above investigations revealed a significant correlation between the fracture's proportion of fibrous and radial regions and impact energy. A typical fracture morphology with a higher proportion of fibrous region and a lower proportion of radial region corresponds to good fracture toughness of the welded joint, presenting a ductile fracture. Conversely, a lower proportion of the fibrous region and a higher proportion of the radial region results in low fracture toughness, showing a cleavage fracture microstructure. Controlling the proportion of the fibrous and radial regions can obtain good microstructural characteristics resembling quasi-cleavage fractures or tough-brittle mixed fractures.

Discussion

Feasibility of the Proposed Method for Reducing Welding Production Cycles

The experimental results presented in the sections "Macroscopic of Weld Beads with Different Welding Procedures" and "Impact Toughness of Welded Joints" demonstrate that the impact toughness of the weld joints welded using the DF-modulated P-GTAW followed by the SAW technique met the requirements of the ASME standard for pressure vessels. Moreover, the weld joint achieved a penetration depth of 5 mm in a single welding operation, approximately 2.5 times deeper than traditional GTAW root pass welding. The deep penetration mechanism, facilitated by the dual-frequency modulated pulse arc, was attributed to the high-frequency pulse electromagnetic compression effect. This effect imparts higher energy density and stronger arc penetration, leading to the easy formation of a liquid metal film at the bottom of the weld pool and the subsequent formation

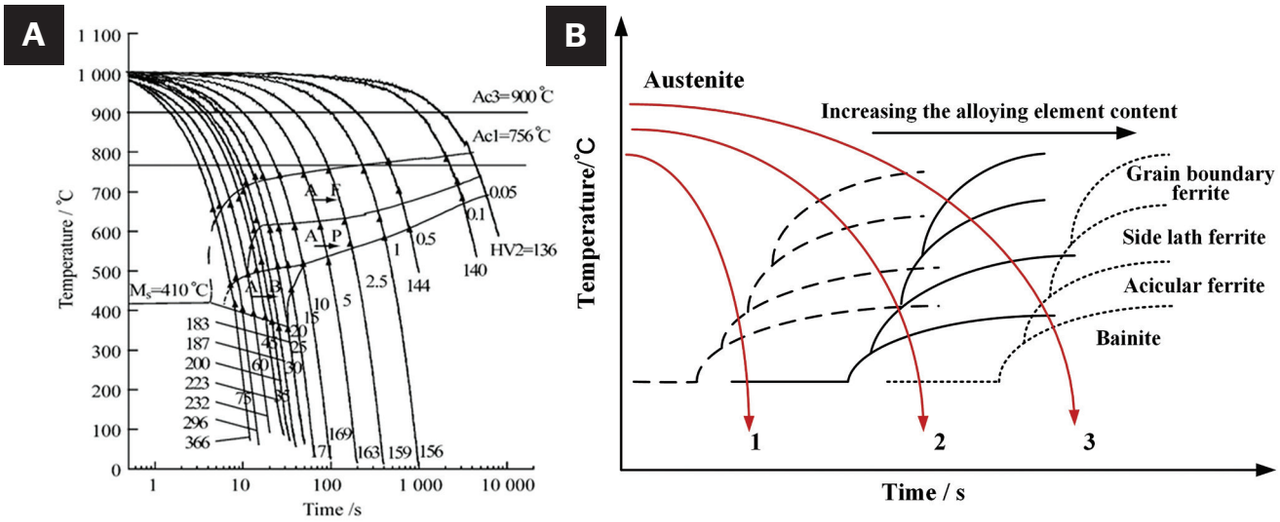

Fig. 10 — CCT curve of A516 Grade 70 steel: A — CCT diagram (Ref. 39); B — CCT changed with different alloying elements.

of a keyhole. Simultaneously, the dual-frequency modulated pulse arc mitigated energy fluctuations in the liquid metal at the top and bottom of the weld pool, enhanced the thermal inertia of the weld pool, effectively reduced the solidification rate, increased the depth of fusion, and provided favorable thermodynamic balance conditions for single-side welding with double-face forming of the weld pool. These observations are supported by published literature (Ref. 38). Additionally, the time required to complete the root pass welding was significantly shorter compared to conventional manual GTAW operations, with a potential reduction of up to 45%. Consequently, this new approach holds promise as a promising application.

By analyzing the measurement data listed in Table 6, it becomes evident that achieving a deep-penetrated root pass weld bead is crucial, as filler and cap welding play a pivotal role in determining the final mechanical properties of the welded joints. It is well-established that the mechanical properties of a weld bead are closely linked to its microstructure, which evolves during the welding process. Therefore, a thorough investigation of the microstructural evolutions of the welds is essential to understanding the relationship between thermal cycle processes, microstructure, and properties.

Analysis of Impact Toughness Between Weld Metal and HAZ

In Fig. 5, it is evident that a small amount of W structure formed within the weld metal of the root pass weld, potentially leading to a reduction in the impact toughness of the welded joint. This phenomenon can be attributed to the application of a high heat input during the root pass welding process to achieve a deep penetration. Nevertheless, the heat dissipation in the root pass was optimal, resulting in an elevated cooling rate of the weld pool and the subsequent formation of W structures. These structures can be effectively eliminated by controlling the filler welding energy. Thereby, it is imperative to optimize the microstructure of the root pass weld bead through choosing an appropriate filler welding procedure.

The microstructural transformation occurring at the center of the weld joint was regulated by the solid-state phase transition involving the continuous transformation of supercooled austenite, with the cooling rate serving as the primary influencing factor, and the continuous cooling transformation (CCT) curve of A516 Grade 70 steel is shown in Fig. 10.

When the two filler passes were employed in the filler welding process, the weld metal exhibited a relatively high cooling rate, and the phase transmission changed with the trajectory of cooling curve 3. As a result, ferrite preferentially nucleated and grew at the austenite grain boundaries. As the temperature continued to decrease, the phase growth of the PF(G) slowed and initiated growth into the grain interior with a lateral plate shape, leading to the formation of the W structure. With further reduction in the temperature, the growth of the W structure slowed. Subsequently, the retained austenite within the grain rapidly nucleated and transformed into fine AF structures. A low heat input welding also resulted in a low dilution rate from the base material, leading to a reduction in the content of alloy elements in the weld and making it easier for austenite grains to grow and fail to achieve fine-grained strengthening. However, the impact toughness of the weld metal primarily depends on the proportion of AF and PF(G), and an increased proportion of AF enhances the impact toughness. Conversely, the increasing proportion of coarse PF(G) will reduce the proportion of AF, which will diminish the hindering effect of grain boundaries on dislocation motion, ultimately leading to a decline in the overall strength of welded joints. Furthermore, the continuous network-like distribution of coarse PF(G) along grain boundaries provides low-resistance propagation pathways for cracks. This microstructural configuration significantly reduces the impact absorption energy of the welds by promoting rapid crack extension under dynamic loading conditions. Finally, the grain boundary strength was weakened, and the impact toughness of the weld metal deteriorated.

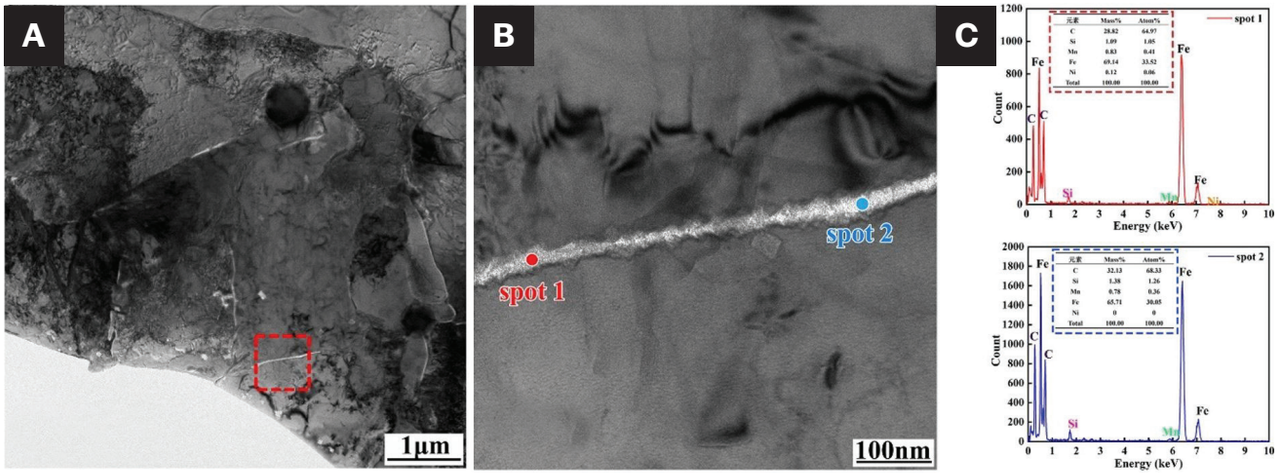

Fig. 11 — TEM images of weld metal (Experiment 2): A — Microstructure; B — overview image; C — EDS results.

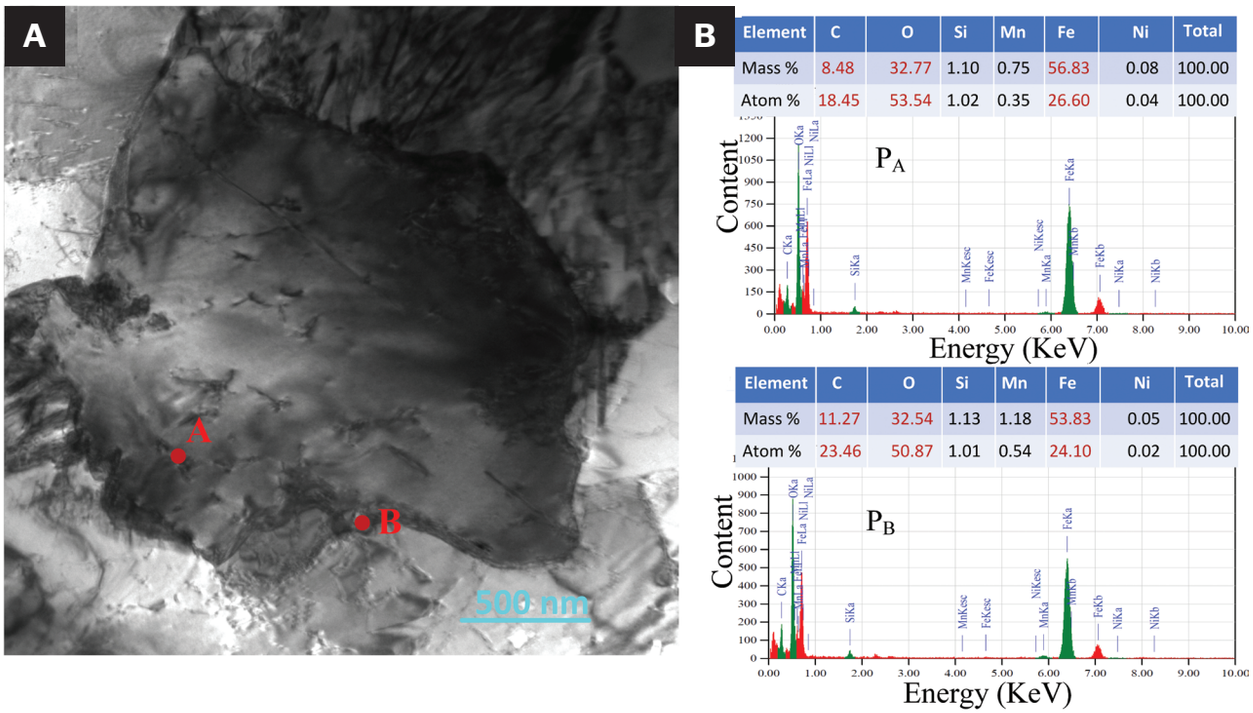

Fig. 12 — TEM images of weld metal (Experiment 1): A — Microstructure; B — EDS results.

In one-pass filler welding, the large heat input made much more base metal dilute into the weld pool, and the numerous alloying elements from the filler wire and flux fused into the weld pool, and then the base metal composition was diluted, causing a shift to the left in the eutectoid component point. This alteration might hinder the planar growth of PF(G) and side-plate ferrite. The inclusion of alloying elements in the weld metal effectively pinned the austenite grain boundaries. Investigations demonstrated that the pinning effect of inclusions and precipitates on the austenite grain boundary, alongside its influence on AF nucleation, significantly contributed to grain refinement (Refs. 40, 41). It is inferred from Fig. 9B(D) that the average size of dispersed inclusion particles was smaller, robustly pinning the grain boundaries and impeding the growth of austenite grains at higher temperatures. Hence, this increased the grain boundary area of the austenite, promoting the grain boundary reaction. Fine PF(G) was eventually formed without significantly compromising the grain boundary strength at lower cooling rates. To further clarify the reasons that the impact toughness of the Nos. 2 and 3 weld metals were inferior to that of the No. 1, the No. 2 weld metal underwent observation using a transmission electron microscope, as illustrated in Fig. 11.

It was observed from Fig. 11 that a white banded film was generated at the grain boundaries; point component analysis indicated that the primary elements were Fe and C, with

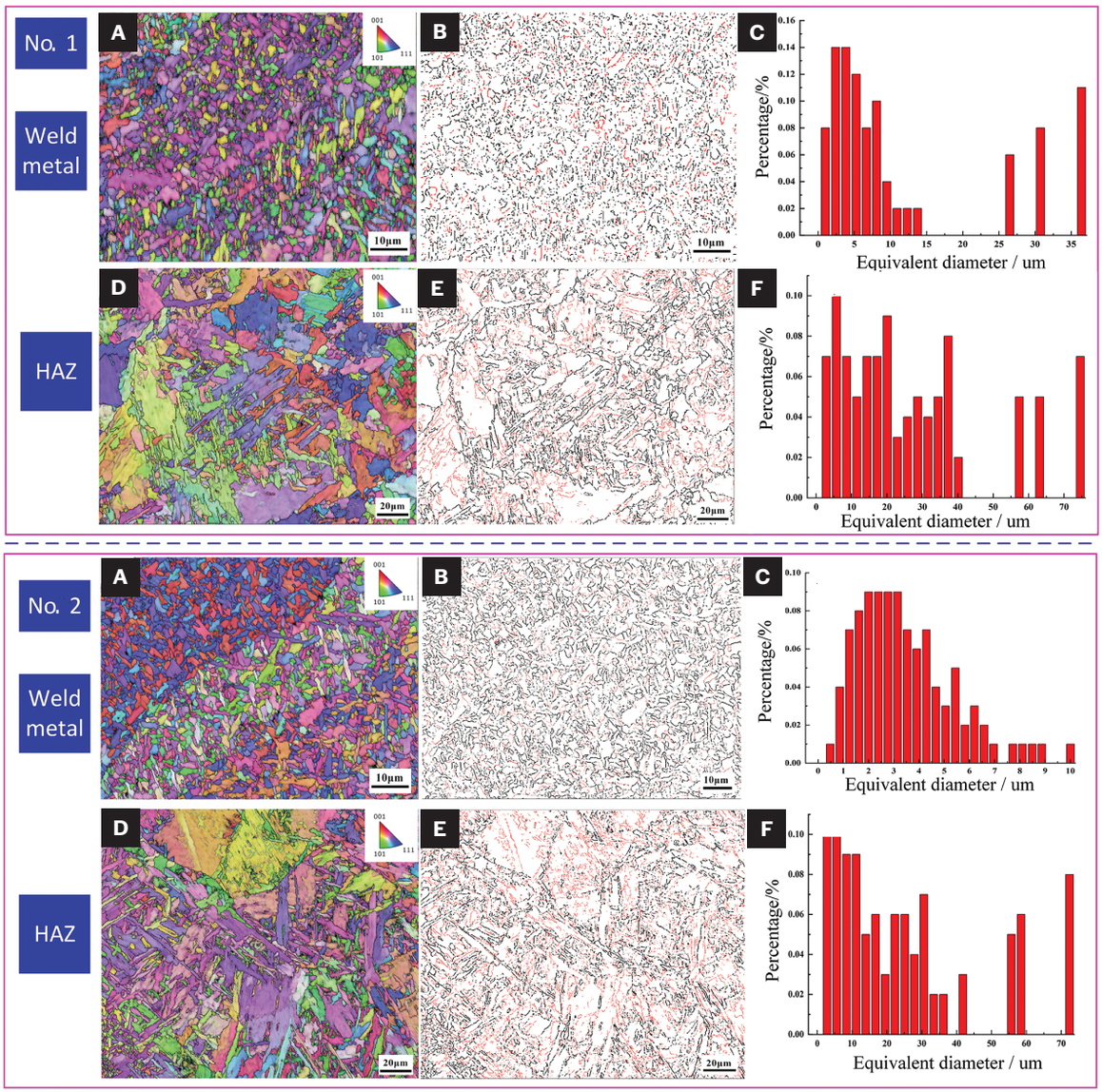

Fig. 13 — EBSD results of weld metal and HAZ under different heat input: A–C — Grain orientation map, proportion chart of low/high-angle grain boundaries, and grain size distribution chart in weld metal; D–F — grain orientation map, proportion chart of low/high-angle grain boundaries, and grain size distribution chart in HAZ.

a small amount of Si, Mn, and Ni. Among these, Fe served as the base element with the highest content, while C was also present in significant quantities due to its tendency to segregate at grain boundaries during the phase transformation, resulting in a relatively higher concentration of C at these boundaries and forming a supersaturated state. And then, the carbide preferentially nucleated at the grain boundary because of the grain boundary structural defects, local high carbon concentration, and rapid diffusion of the C atom. As cooling time increased, a large number of carbides were precipitated in the grain boundary, equivalent to a hard and brittle carbide shell wrapped around the grains. At the same time, the precipitation of carbides in the grain boundary caused the concentration of carbon and alloying elements in the steel matrix to decrease, which weakened the solid solution strength of the matrix near the grain boundary. Consequently, many carbides precipitated and aggregated at the grain boundary, causing cracks to be more easily initiated during impact tests, and then the generated cracks propagated along the grain boundary, which finally tore the weld metal. Therefore, the impact toughness of the weld metal decreased. Moreover, during the deformation process of impact testing, the carbide hard shell at the boundary was fractured, which resulted in an observable tearing ridge (Fig. 9A(D)). However, no similar microstructural morphology was observed in the weld metal in a single-pass welding condition (Experiment 1).

Figure 12 illustrates that the discontinuous block-shaped phase structures formed at the grain boundaries. Point component analysis indicated that the block-shaped structures

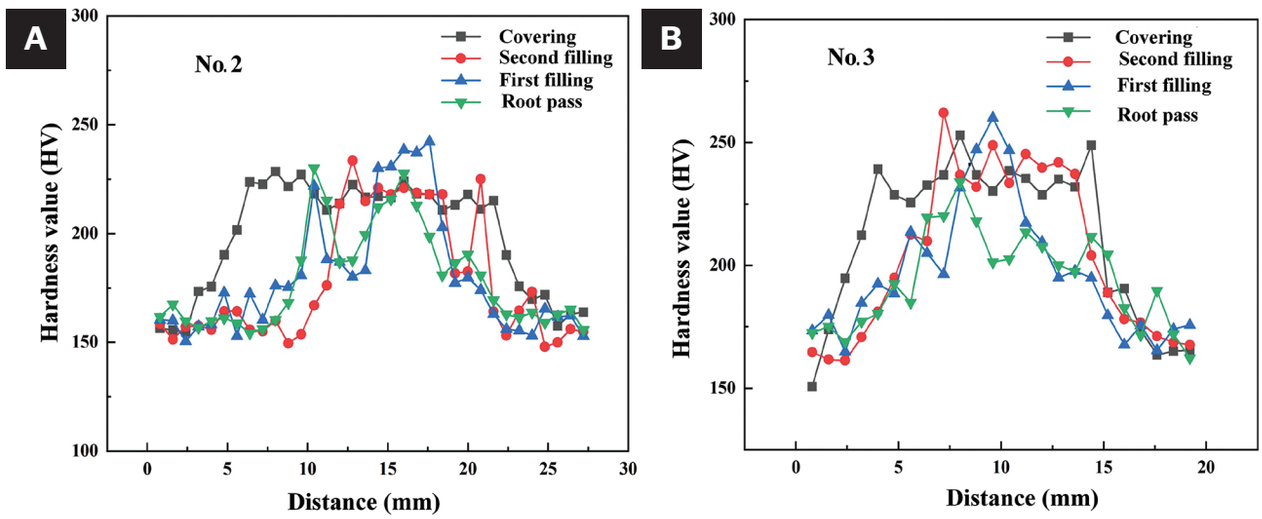

Fig. 14 — Microhardness of weld joint with different filler welding procedures: A — Experiment 2; B — Experiment 3.

primarily contained the elements C, O, and Fe, with minor amounts of Si, Mn, and Ni. Hence, in the one-pass filler welding condition, the phases generated at the grain boundaries may have consisted of carbides with a block shape and oxides, such as MnO or SiO_2. A small number of oxides can pin the austenite grain boundaries, inhibiting the growth of austenite grains, thereby refining the weld microstructure and enhancing the toughness of the weld metal. Meanwhile, owing to the carbide's exceptional hardness and strength, small-sized block-shaped carbides function as highly effective barriers, impeding the initiation of cracks at grain boundaries. By exerting a pinning effect, these carbides reinforce the grain boundaries, thereby enhancing their overall strength. Moreover, they play a crucial role as obstacles in crack extension, significantly increasing the resistance encountered by cracks during their extension process. Additionally, these carbides can modify the path of crack extension, shifting it from a straight, planar expansion to a zigzag pattern. Thereby, the impact toughness of weld metal in Experiment 1 was higher than that of Experiments 2 and 3.

The proportions of low- and high-angle grain boundaries, as well as the grain sizes and orientations, within both the weld metal and the HAZ of the specimens, were measured and subjected to a comparative analysis utilizing the EBSD technique. The results are shown in Fig. 13.

Figure 13 illustrates that the first specimen exhibited a proportion of high-angle grain boundaries in the weld metal of 72.8%, with an average grain size of 1.6 μm. In the HAZ, the proportion of high-angle grain boundaries was 43.6%, and the average grain size was 5.2 μm. As in the above analysis, the weld metal contained an amount of AF, which radiated and grew in various directions from its nucleation points. The structure of AF is characterized by an interlocking mechanism, with adjacent grains exhibiting large misorientation angles. This distribution effectively hinders the crack extension, resulting in a higher impact toughness in the weld metal than the HAZ. However, in the second specimen, the proportion of high-angle grain boundaries in the weld metal was 56.4%, with an average grain size of 3.8 μm. In contrast, the HAZ showed a proportion of high-angle grain boundaries of 76.6%, with an average grain size of 3.2 μm, representing a higher impact toughness than that of weld metal. Consequently, through precise control of heat input, a microstructure characterized by a high proportion of high-angle grain boundaries and fine grain size could be obtained, leading to a substantial improvement in the impact toughness of the welded joint.

To systematically investigate the toughness discrepancy between the WM and the HAZ, microhardness testing was also conducted across the weld joint regions. Figure 14 shows three critical observations: 1) The WM exhibited an 11.2% lower average microhardness (206 $\pm$ 12 HV) compared to the HAZ (232 $\pm$ 12 HV); 2) The HAZ demonstrated greater microhardness variability (175 HV–241 HV) versus the WM (175 HV–220 HV); 3) Peak microhardness values (232 $\pm$ 8 HV) consistently occurred in the coarse-grained HAZ. This positive correlation between microhardness and impact toughness aligned with the extended HAZ morphology presented in Fig. 3, suggesting that localized hardening mechanisms in specific HAZ subzones may improve ductility, which has been investigated and reported by Mackenzie Boeing Jorgensen Smith (Ref. 42).

In Fig. 4, it is apparent that the impact toughness of the HAZ seemed to be a consequence of heat input, specifically welding current. It was fitted through polynomial fitting and displayed the black curve, expressed by the equation $y = 19.3 + 45.9x + 1.3x^2$, where y denotes toughness and x symbolizes the welding current. This fitted equation offers a valuable method for predicting variations in the impact toughness of the HAZ concerning varying heat input. However, the impact toughness of the weld metal of the welded joint cannot be predicted by the fitted curve because the variation of impact toughness depends not only on heat input from the filler and covering welding process as well as root pass welding but also the content of the alloying elements and the phases formed at the grain boundary, which cannot be quantitatively characterized in the welding process and the

weld metal. Consequently, it is very difficult to fit the curve between the impact toughness of the weld metal and the processing parameters.

Conclusions

Medium-thick A516 Grade 70 steel plates were successfully welded using a novel method, and subsequent analyses were conducted on the microstructure and impact toughness of the weld joints. The primary conclusions are as follows:

1. The DF-modulated P-GTAW technique, followed by SAW, successfully achieved a fully penetrated root pass weld bead with a depth of 5 mm without backing, approximately 2.5 times deeper than conventional GTAW root pass welding. This significantly reduced welding time, reducing by approximately 45% for 3m^3 nuclear pressure vessels.

2. Control of heat input in the SAW process not only controls microstructures in the SAW region but also in the DF-modulated P-GTAW root pass to ensure good toughness, even though none of the filler metal was added to the DF-modulated P-GTAW. When the heat input (14.85 kJ/cm for the initial filler pass, 23.81 kJ/cm for the second filler pass, and 27.37 kJ/cm for the cover pass) was precisely controlled, a sound butt weld joint with high impact toughness was obtained. The impact toughness of the HAZ reached 107 J, and the weld metal exhibited an impact toughness of 35 J, both of which met the ASME standard requirements for nuclear pressure vessels.

3. The microstructure of the weld metal primarily consisted of PF(G) and AF. In one-pass filler welding, the weld metal exhibited refined grains and an increased AF proportion, resulting in superior impact toughness compared to the HAZ. In two-pass filler welding, the carbide films formed on the grain boundaries reduce the strength of the grain boundaries, resulting in a decrease of impact toughness in the weld metal, and the HAZ formed strip-like bainite due to shorter cooling times ($t_{8/5}$ = 10 s), effectively impeding crack extension and enhancing impact toughness.

Acknowledgments

The authors acknowledge the support from the National Natural Science Foundation of China (#52265050), the Lanzhou Youth Science and Technology Innovation Talent Project (#2023-QN-90), the Wenzhou Science and Technology Planning Project (#2023G0157), Gansu Provincial Key Research and Development Program (#25YFGA023), and Innovation Fund for Higher Education Institutions of Gansu Province (#2025A-022).

References

1. Ragavendran, M., Vasudevan, M., and Hussain, N. 2022. Study of the microstructure, mechanical properties, residual stresses, and distortion in Type 316LN stainless steel medium thickness plate weld joints. *Journal of Materials Engineering and Performance* 31: 5013–5025. DOI: 10.1007/s11665-021-06534-1

2. Zhu, Y., Mu, W., Cai, Y., Dong, D., and Wang, M. 2021. A novel high-efficient welding technology with rotating arc assisted by laser and its application for cryogenic steels. *Journal of Manufacturing Processes* 268: 1134–1146. DOI: 10.1016/j.jmapro.2021.06.042

3. Zhu, Z., Zhang, G., Wang, K., Shi, Y., and Fan, D. 2021. Joint penetration monitoring in low-frequency pulsed GTA root pass welding of medium-thick steel plates. *Welding Journal* 100: 281-s to 290-s. DOI: 10.29391/2021.100.025

4. Sharma, G., Tyagi, R., and Sharma, P. 2022. Variants of TIG welding process for improvement of weld penetration depth-A review. *Materials Today: Proceedings* 64: 1362–1366. DOI: 10.1016/j.matpr.2022.04.266

5. Li, Y., Wang, L., and Wu, C. 2019. A novel unified model of keyhole plasma arc welding. *International Journal of Heat and Mass Transfer* 133: 885–894. DOI: 10.1016/j.ijheatmasstransfer.2018.12.130

6. Zhou, W., Jia, C., and Zhou, F. 2023. Dynamic evolution of keyhole and weld pool throughout the thickness during keyhole plasma arc welding. *Journal of Materials Processing Technology* 322: 118206. DOI: 10.1016/j.jmatprotec.2023.118206

7. Bhanu, V., Gupta, A., and Pandey, C. 2022. Role of A-TIG process in joining of martensitic and austenitic steels for ultra-supercritical power plants-a state of the art review. *Nuclear Engineering and Technology* 54: 2755–2770. DOI: 10.1016/j.net.2022.03.003

8. Ma, C., Chen, B., and Meng, Z. 2023. Characteristic of keyhole, molten pool and microstructure of oscillating laser TIG hybrid welding. *Optics & Laser Technology* 161: 109142. DOI: 10.1016 /j.optlastec.2023.109142

9. Sahoo, A., and Tripathy, S. 2021. Development in plasma arc welding process: a review. *Materials Today: Proceedings* 41: 363–368. DOI: 10.1016/j.matpr.2020.09.562

10. Cai, D., Luo, Z., and Han, S. 2023. Plasma characteristics of a novel coaxial laser-plasma hybrid welding of Ti alloy. *Optics and Lasers in Engineering* 167: 107599. DOI: 10.1016/j.optlaseng.2023.10759

11. Yang, L., Geng, S., and Jiang, P. 2024. Investigation on the keyhole/molten pool dynamic behavior during adjustable ring-mode laser welding of medium-thick aluminum alloy. *International Journal of Thermal Sciences* 196: 108723. DOI: 10.1016/j.ijthermalsci.2023.108723

12. Kanchan, P., and Patil, D. V. 2013. A review on GTAW technique for high strength aluminium alloys (AA 7xxx series). *International Journal of Engineering and Research Technology* 2(8): 2477–2490.

13. Dong, Z. H., Tian, Y., Zhang, L., Jiang, T., Wang, D. F., Chang, Y., and Chen, D. G. 2025. Research status of high efficiency deep penetration welding of medium-thick plate titanium alloy: A review. *Defence Technology* 45: 175–202.

14. Saedi, H. R., and Unkel, W. 1988. Arc and weld pool behavior for pulsed current GTAW. *Welding Journal* 67(11): 247-s to 256-s.

15. Qi, B. J., Yang, M. X., Cong, B. Q., and Liu, F. J. 2013. The effect of arc behavior on weld geometry by high-frequency pulse GTAW process with 0Cr18Ni9Ti stainless steel. *The International Journal of Advanced Manufacturing Technology* 66: 1545–1553.

16. Zhao, H. Y., Xing, Y., Zhang, J. Z., Chen, S. J., Yu, Y., He, G. P., and Lv, T. 2025. Morphology and energy distribution characteristics of ultra-high frequency adjustable multi-pulse GTAW arc. *Journal of Manufacturing Processes* 142: 30–43.

17. Hariprasath, P., Sivaraj, P., and Balasubramanian, V. 2022. Effect of the welding technique on mechanical properties and metallurgical characteristics of the naval grade high strength low alloy steel joints produced by SMAW and GMAW. *CIRP Journal Manufacturing Science Technology* 37: 584–595. DOI: 10.1016/ j.cirpj.2022.03.007

18. Han, S., Shin, S., and Lee, S. 2009. Effect of cooling conditions on microstructures and mechanical properties in API X80 line pipe steels. *Korean Journal of Metals and Materials* 47: 523–532.

19. Gu, Y., Lu, N., Xu, Y., Shi, Y., Zhang, G., and Sun, Q. 2023. Microstructure characteristics of Q345R-steel welded joints and their corrosion behavior in a hydrofluoric acid environment. *Journal of Nuclear Materials* 574: 154214. DOI: 10.1016/j.jnucmat.2022.154214

20. Jiang, C., Wang, X., Du, Y., and Wang, W. 2021. Analysis for the welding crack leakage of deethanizer. *Journal of Physics Conference Series* 1885(3): 032038.

21. Pan, J., Zeng, C., and Hong, Z. 2019. A novel method to estimate the fracture toughness of pressure vessel ferritic steels in the ductile to brittle transition region using finite element analysis and master curve method. *International Journal of Pressure Vessels and Piping* 176: 103949. DOI: 10.1016/j.ijpvp.2019.103949

22. Cui, Q., Hui, H., and Li, P. 2015. Applicability of the ASME exemption curve for Chinese pressure vessel steel Q345R. *Journal of Pressure Vessel Technology* 137: 061602. DOI: 10.1115/1.4030673

23. Chen, Z., Pan, J., and Jin, T. 2018. Estimation of fracture toughness of 16MnDR steel using Master Curve method and Charpy V-notch impact energy. *Theoretical and Applied Fracture Mechanics* 96: 443–451. DOI: 10.1016/j.tafmec.2018.06.007

24. Xuan, C., and Mu, W. 2022. New insights of heterogeneous nucleation and anisotropic growth of acicular ferrite on non-metallic inclusion. *Materials & Design* 221: 110892. DOI: 10.1016/j.matdes.2022.110892.

25. Loder, D., Susanne, K., and Bernhard, C. 2017. Acicular ferrite formation and its influencing factors-A review. *Journal of Materials Science Research* 6: 24–43.

26. Lv, S., Wu, H., and Wang, K. 2023. The microstructure evolution and influence factors of acicular ferrite in low alloy steels. *Computational Materials Science* 218: 111989. DOI: 10.1016/j.commatsci.2022.111989

27. Luo, X., Chen, X., and Wang, T. 2018. Effect of morphologies of martensite–austenite constituents on impact toughness in intercritically reheated coarse-grained heat-affected zone of HSLA steel. *Materials Science and Engineering: A* 710: 192–199. DOI: 10.1016/j.msea.2017.10.079

28. Huda, N., Wang, Y., and Li, L. 2019. Effect of martensite-austenite (MA) distribution on mechanical properties of inter-critical reheated coarse grain heat affected zone in X80 line pipe steel. *Materials Science and Engineering: A* 765: 138301. DOI: 10.1016/j.msea.2019.138301

29. Li, X., Fan, Y., and Ma, X. 2015. Influence of martensite–austenite constituents formed at different intercritical temperatures on toughness. *Materials & Design* 67: 457–463. DOI: 10.1016/j.matdes. 2014.10.028

30. He, Q., Hu, X., and Sun, Q. 2022. Characterization of heterogeneous microstructure and mechanical properties of Q345R welded joints including roles of the welding process. *Metals* 12: 1708. DOI10.3390/met12101708

31. Steel-Iron Material Table 088 Appendix 2: Fine-Grained Steel Suitable for Welding. *Processing Guide, Especially for Fusion Welding: Determine the Cooling Time t8/5 for the Welding Temperature Cycle Marking*. October 1993. Issue 4. Verlag Stahleisen, Dusseldorf, Germany.

32. St-Laurent, S., and L'Espérance, G. 1992. Effects of chemistry, density and size distribution of inclusions on the nucleation of acicular ferrite of C-Mn steel shielded-metal-arc-welding weldments. *Materials Science and Engineering: A* 149(2): 203–216. DOI:10.1016/0921-5093(92)90381-A

33. Zhang, D., Terasaki, H., and Komizo, Y. I. 2010. In situ observation of the formation of intragranular acicular ferrite at non-metallic inclusions in C–Mn steel. *Acta Materialia* 58(4): 1369–1378. DOI: 10.1016/j.actamat.2009.10.043

34. Xuan, C. J., and Mu, W. Z. 2022. New insights of heterogeneous nucleation and anisotropic growth of acicular ferrite on non-metallic inclusion. *Materials & Design* 221: 110892. DOI: 10.1016/j.matdes. 2022.110892

35. Kang, Y., Jeong, S., and Kang, J. H. 2016. Factors affecting the inclusion potency for acicular ferrite nucleation in high-strength steel welds. *Metallurgical and Materials Transactions A* 47: 284–2854. DOI: 10.1007/s11661-016-3456-0

36. Almar-Naess, A., Haagensen, P. J., Lian, B., Moan, T., and Simonsen, T. 1984. Investigation of the Alexander L. Kielland failure—Metallurgical and fracture analysis. *Journal of Energy Resources Technology, Transactions of the ASME* 106(1): 24–31.

37. Matthews, J. R. 1996. On the relationship between shear lip, shear index and energy in dynamic tear specimens. *Engineering Fracture Mechanics* 54(1): 11–23.

38. Zhang, G., Xu, Z., Shi, Y., Zhu, M., and Fan, D. 2023. Analysis of arc-weld pool behavior of double-frequency modulated pulse TIG root pass welding. *Journal of Mechanical Engineering* 59(12): 245–252.

39. Li, H. Y., Ding, C. W., Zhang, X. W., and Yu, Z. J. 2007. Continuous cooling transformation curve of under cooling austenite about 16MnR Steel. *Journal of Materials Science and Engineering* 25(5): 727–730. DOI:10.14136/ j.cnki.issn 1673-2812.2007.05.034

40. Wan, X., Wu, K., and Huang, G. In situ observation of austenite grain growth behavior in the simulated coarse-grained heat-affected zone of Ti-microalloyed steels. *International Journal of Minerals, Metallurgy, and Materials* 21(9): 878–885. DOI: 10.1007/s12613-014-0984-8

41. Lin, C., Su, Y., and Wang, W. 2018. On pinning effect of austenite grain growth in Mg-containing low-carbon steel. *Materials Science and Technology* 34: 596–606. DOI: 10.1080/02670836.2017.1421037

42. Jorgensen Smith, M. B. 2021. The correlation of hardness to toughness and the superior impact properties of martensite in pressure vessel steels applied to temper bead qualification. Ph.D. diss., The Ohio State University.

GANG ZHANG (*zhanggang@lut.edu.cn*), **BING ZHANG**, **NA LV**, **YOUWEI XU**, **YUFEN GU**, and **YU SHI** are with State Key Laboratory of Advanced Processing and Recycling Non-ferrous Metals, Lanzhou University of Technology, Lanzhou, China. **ZHANG** is also with the Wenzhou Engineering Institute of Pump and Valve, Lanzhou University of Technology, Wenzhou, China.